# Robust picosecond writing of a layered antiferromagnet by staggered spin-orbit fields

P. E. Roy,[1,*] R. M. Otxoa,[1,†] and J. Wunderlich[1,2]

[1]*Hitachi Cambridge Laboratory, J J Thomson Avenue, Cambridge CB3 0HE, United Kingdom*

[2]*Institute of Physics ASCR, v.v.i., Cukrovarnicka 10, 162 53 Praha 6, Czech Republic*

(Received 21 April 2016; revised manuscript received 27 June 2016; published 28 July 2016)

Ultrafast electrical switching by current-induced staggered spin-orbit fields, with minimal risk of overshoot is shown in layered easy-plane antiferromagnets with basal-plane anisotropies. Reliable switching is due to the fieldlike torque, relaxing stringent requirements with respect to precision in the duration of the excitation pulse. Focus is put on a system with weak planar biaxial anisotropy. We investigate the switching as a function of the spin-orbit field strength, pulse duration, rise and fall times, and damping using atomistic spin dynamics simulations and an effective equation for the antiferromagnetic order parameter. The critical spin-orbit field strength required for switching a biaxial system is determined, and we show that writing is possible at feasible current magnitudes. Finally, we discuss switching of systems exhibiting a dominant uniaxial basal-plane anisotropy.

DOI: 10.1103/PhysRevB.94.014439

## I. INTRODUCTION

The inherent properties of antiferromagnets (AFMs) such as ultrafast dynamics, zero net moment, and insensitivity to external magnetic stray fields make them candidates for high speed memory devices. Because AFMs exhibit anisotropic magnetoresistance (AMR), electrical detection of the AFM state is possible [1]. The writing operation, i.e., reorientation of the AFM sublattice magnetizations has been subject to several proposals, including using short laser pulses [2–4] and spin transfer torque (STT) induced by an impinging spin accumulation either by the spin Hall effect at a heavy metal/AFM interface [5] or by injection from a coupled ferromagnet [6,7]. Similar to STT in ferromagnetic (FM) devices, a carrier spin accumulation $\mathbf{s}$, with initial polarization $\mathbf{p}$, interacting with a magnetic moment $\mathbf{m}$, mainly gives rise to two situations: For short carrier spin lifetime relative to the spin-precession time, $\mathbf{s} \propto \mathbf{p}$, and for long spin lifetimes, $\mathbf{s} \propto \mathbf{m} \times \mathbf{p}$. In an AFM with sublattices $A, B$, the torque on $A, B$ is $\partial_t \mathbf{m}_{A,B} \propto \mathbf{m}_{A,B} \times \mathbf{s}$, where $\mathbf{m}_{A,B}$ is the magnetic moment of sublattices $A$, $B$, respectively, $\mathbf{m}_A = -\mathbf{m}_B$, and $\partial_t$ denotes the time derivative. Thus, two types of torques may be present [8]; $\partial_t \mathbf{m}_{A,B} \propto \mathbf{m}_{A,B} \times \mathbf{p}_{A,B}$ or $\partial_t \mathbf{m}_{A,B} \propto \mathbf{m}_{A,B} \times (\mathbf{m}_{A,B} \times \mathbf{p}_{A,B})$, where the former is a fieldlike torque, the latter is an antidamping torque, and $\mathbf{p}_{A,B}$ is the initial polarization of $\mathbf{s}$ on $A$ and $B$, respectively. If $\mathbf{p}_{A,B} = \mathbf{p}$ the local field $H_{A,B} \propto \mathbf{p}$, and thus this torque is not efficient. The antidamping torque, however is due to the local field $\mathbf{H}_{A,B} \propto \mathbf{m}_{A,B} \times \mathbf{p}$. Such a field is staggered, i.e., alternating in sign between $A$ and $B$ and couples efficiently to torque the AFM.

However, in switching an AFM by the antidamping torque, an overshoot of the targeted written state is a viable risk, unless care is taken with respect to pulse duration [5]. This is because the torque is always rotating the magnetization while the current is on. Furthermore, several theoretical studies focus on driving AFM domain walls (DWs) by means of STT [9–12]. These works have been important in predicting the possibility of current-induced excitations in AFMs. However, unless the type of DWs considered in those works can be controllably formed and their position easily detected, a device with moving AFM DWs as the mode of operation is at present unlikely. For a robust device, electrical manipulation, whereby the AFM order parameter is switched fast and controllably between two stable minima, without any coupled FMs is a desirable route to follow. Also, for easy AMR detection of the written state, a system whereby the AFM order switches between two orthogonal directions is preferable. Thus, materials with inherent biaxial magnetocrystalline anisotropy are good candidates for a memory device.

In crystals with locally broken inversion symmetry at magnetic sites and where $A$ and $B$ form inversion partners, another possibility for AFM spin-axis reorientation was proposed in Ref. [13]. There, the inverse spin galvanic effect [14] produces a staggered local $\mathbf{s}$, with $\mathbf{p}_A = -\mathbf{p}_B$. In this case, it is the local field $\mathbf{H}_{A,B} \propto \mathbf{p}_{A,B}$ which is staggered. Thus it is here the fieldlike torque which efficiently drives the AFM switching process. These conditions can be generated by an electrical current density $\mathbf{j}$, injected perpendicular to the axis of locally broken inversion symmetry. Proposed materials to this end are to date $Mn_2Au$ and CuMnAs [13,15–22]. Experimental indication of the electrical manipulation of the AFM state in a multidomain CuMnAs sample by the fieldlike torque has recently been reported [21].

In this paper, we show reliable ultrafast switching of a $Mn_2Au$ device whose crystal structure [23] is shown in Fig. 1(a). This system has a magnetically hard axis along the $c$ axis and biaxial anisotropy in the basal planes with easy directions along the [110] and [1$\bar{1}$0] axes [13,24]. Mn atoms occupy sites $A$ and $B$ [Fig. 1(a)]. Typical basal-plane domain sizes are ∼500 nm [22]. So, for a homogeneous Neel ordered state the lateral dimensions of a thin film device should be ⩽500 nm. A current injected parallel to the basal planes generates a staggered SO field as $\mathbf{H}_A^{SO} \sim +\hat{\mathbf{z}} \times \mathbf{j}$ (at sublattice $A$) and $\mathbf{H}_B^{SO} \sim -\hat{\mathbf{z}} \times \mathbf{j}$ (at sublattice $B$) [13], giving rise to fieldlike torques. To effectively switch the spin axes of the sublattices between two stable minima, the biaxial easy directions should coincide with the current directions. We thus consider the geometry in Fig. 1(b) [13]. Recent calculated values of $|\mathbf{H}^{SO}|$ for $Mn_2Au$ are ∼20 Oe per $10^7$ A/cm$^2$ (slightly lower than for CuMnAs) [21].

*per24@cam.ac.uk

†ro274@cam.ac.uk

 

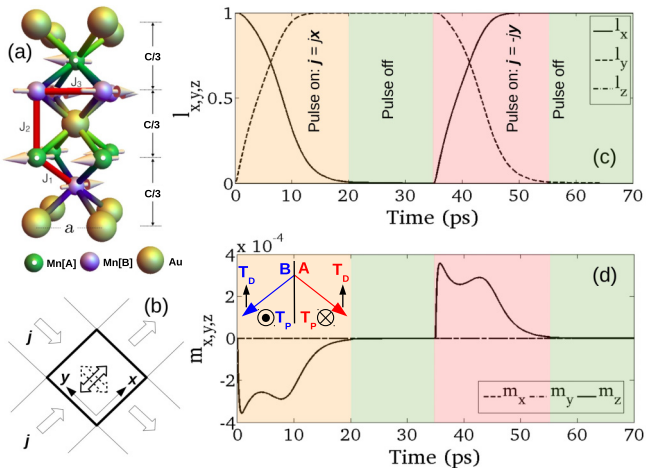


FIG. 1. (a): Crystal and spin structure of $Mn_2Au$ with basal-plane lattice parameter $a = 3.328$ Å, $c = 8.539$ Å. The bond-exchange constants $J_{1,2,3}$ used are marked by red solid lines. The Mn atoms occupy two types of sites, $A$ and $B$ (see the key). (b): Coordinate system and orientation of a square device. Current ($\mathbf{j}$) injection directions are indicated by large arrows, and two stable positions of the antiferromagnetic sublattices are shown by double arrows in the device. $+\hat{\mathbf{z}}$ is along the outward paper normal. (c) and (d): Atomistic spin dynamics results of the time evolution of $\mathbf{l}$ (c) and $\mathbf{m}$ (d) during two writing operations as described in the text. Inset in (d): vector diagram of the precessional and damping exchange torques, $\mathbf{T}_P$ and $\mathbf{T}_D$, respectively, on sublattices $A$ ($\mathbf{T}_P||+\hat{\mathbf{y}}$, $\mathbf{T}_D||+\hat{\mathbf{z}}$) and $B$ ($\mathbf{T}_P||-\hat{\mathbf{y}}$, $\mathbf{T}_D||+\hat{\mathbf{z}}$).

## II. ATOMISTIC SPIN DYNAMICS SIMULATION OF THE WRITING OPERATION

### A. Method and system parameters

For modeling the device, the total energy, comprised of exchange, tetragonal anisotropy, and Zeeman energies is:

$$E = -\sum_{i,j\in N_i} J_{ij}\mathbf{m}_i\cdot\mathbf{m}_j - K_{2\perp}\sum_i(\mathbf{m}_i\cdot\hat{\mathbf{u}}_3)^2 - \frac{K_{4\perp}}{2}\sum_i(\mathbf{m}_i\cdot\hat{\mathbf{u}}_3)^4 - \frac{K_{4\parallel}}{2}\sum_i(\mathbf{m}_i\cdot\hat{\mathbf{u}}_1)^4 - \frac{K_{4\parallel}}{2}\sum_i(\mathbf{m}_i\cdot\hat{\mathbf{u}}_2)^4 - \mu_0\mu_s\sum_i\mathbf{m}_i\cdot\mathbf{H}_i^{\mathrm{SO}}, \quad (1)$$

where $\mathbf{m}$ is the unit magnetic moment at site $i$, $\mu_0$ the magnetic permeability in vacuum, and $\mu_s$ the saturation magnetic moment. The first term in Eq. (1) is the exchange energy with coupling constants $J_{ij}$ between moments $i$ and $j$. Terms two, three, four, and five constitute the magnetocrystalline anisotropy energy with $K_{2\perp}$, $K_{4\perp}$, and $K_{4\parallel}$ being the second order perpendicular, fourth order perpendicular, and fourth order in-plane anisotropy constants, respectively. Unit vectors $\hat{\mathbf{u}}_{1,2,3}$ denote easy directions. The sixth term is the Zeeman energy with $\mathbf{H}_i^{\mathrm{SO}}$ being the current-induced staggered SO field.

The equation of motion for $\mathbf{m}_i$ in the presence of interaction fields $\mathbf{H}_i$ is given by the explicit (for computational purposes) Landau-Lifshitz-Gilbert equation [25]:

$$(1+\alpha^2)\frac{\partial\mathbf{m}_i}{\partial t} = -\gamma\mathbf{m}_i\times\mathbf{H}_i - \alpha\gamma\mathbf{m}_i\times(\mathbf{m}_i\times\mathbf{H}_i). \quad (2)$$

Here, $\gamma = 2.21\times10^5$ m(As)$^{-1}$ is the gyromagnetic ratio, $\alpha$ is the damping parameter, and $\mathbf{H}_i$ is evaluated from Eq. (1) as $\mathbf{H}_i = \frac{-1}{\mu_0\mu_s}\frac{\partial E}{\partial\mathbf{m}_i}$. We start out by trying the switching capability of the device in Fig. 1(b) using atomistic spin dynamics simulations [26]. The size here is $150\times150\times5$ unit cells ($49.2\times49.2\times4.2695$ nm$^3$) of $Mn_2Au$. Exchange couplings used are $J_1 = -396k_B^{-1}$ K, $J_2 = -532k_B^{-1}$ K, and $J_3 = 115k_B^{-1}$ K [15,17,27] (where $k_B$ is the Boltzmann constant). For the biaxial basal-plane ansiotropy, $K_{4\parallel}$ corresponds to an anisotropy field of 100 Oe [17]; $K_{4\parallel}$ is here then $1.8548\times10^{-25}$ J. $K_{2\perp}$ and $K_{4\perp}$ per Mn ion is taken from Ref. [16]; we set $K_{2\perp} = -1.303\times10^{-22}$ J and $K_{4\perp} = 2K_{4\parallel}$. Here, $\alpha = 0.01$, $\mu_s = 4\mu_b$ [17], where $\mu_b$ is the Bohr magneton. Considering the device in Fig. 1(b), $\hat{\mathbf{u}}_1 = \hat{\mathbf{x}}$, $\hat{\mathbf{u}}_2 = \hat{\mathbf{y}}$ and $\hat{\mathbf{u}}_3 = \hat{\mathbf{z}}$. Equation (2) is then solved by a fifth order Runge-Kutta scheme [28]. Two current pulses are applied: The first pulse aims to switch the $A$ ($B$) sublattice from being parallel (antiparallel) to $\hat{\mathbf{x}}$ into directions parallel (antiparallel) to $\hat{\mathbf{y}}$, and the second pulse is to switch the sublattices back to their original state; a $\tau_p = 20$ ps square current pulse is sent along $+\hat{\mathbf{x}}$, generating a staggered $\mathbf{H}^{\mathrm{SO}}$ along $+\hat{\mathbf{y}}$ on an $A$ site and along $-\hat{\mathbf{y}}$ on a $B$ site. A waiting time of 15 ps is imposed to verify the stability of the written state. Then, a second pulse along $-\hat{\mathbf{y}}$ is applied, generating a staggered $\mathbf{H}^{\mathrm{SO}}$ parallel (antiparallel) to $\hat{\mathbf{x}}$ on $A$ ($B$) sites. We set $|\mathbf{H}^{\mathrm{SO}}| = 100$ Oe, corresponding to $\sim5\times10^7$ A/cm$^2$. To characterize the state, we use the antiferromagnetic order parameter $\mathbf{l} = \frac{\mathbf{m}_A-\mathbf{m}_B}{2}$ and the magnetization $\mathbf{m} = \frac{\mathbf{m}_A+\mathbf{m}_B}{2}$. As the system is three dimensional, the volume averaged $\mathbf{l}$ and $\mathbf{m}$ are extracted.

### B. Simulation of a switching cycle: result and discussion

Figure 1(c) shows a successful switching cycle. Further, due to the symmetry of the torques, $l_z$, $m_x$, and $m_y$ remain zero at all times. As the SO torque itself is not staggered, a build-up in $m_z$ occurs (Fig. 1(d)); the exchange field due to the associated exchange energy penalty causes a large precessional torque [due to the first term in Eq. (2)] along the $\pm\hat{\mathbf{y}}$ directions. Thus, fast switching is due to an exchange-enhanced torque. The damping part of the exchange torque [second term in Eq. (2)] acts as to restore $m_z$ to zero, i.e., the lower the $\alpha$, the larger the amplitude of $m_z$, leading to shorter switching times and lower SO fields required to achieve a switch. Note here that we have used a quite long $\tau_p$. In order to achieve a switch, $\tau_p$ need only to be long enough to bring $\mathbf{l}$ over the biaxial anisotropy barrier, after which even if the pulse is off, the anisotropy field brings $\mathbf{l}$ to the next minima. The simulation in Figs. 1(c) and 1(d) also shows that even though $\tau_p$ was on for a time longer than that required for a switch, $\mathbf{l}$ did not overshoot the targeted minimum. The reason is the fieldlike SO torque and the direction of $\mathbf{H}^{\mathrm{SO}}$ always being along an easy direction for the geometry in Fig. 1(b). Thus even for a DC current, $\mathbf{l}$ is unlikely to overshoot a targeted minimum.

## III. MACROSPIN APPROACH

There may be, however, some conditions whereby an overshoot event could occur. We therefore investigate the dependence of the final orientation of $\mathbf{l}$ for different $\tau_p$ and $|\mathbf{H}^{\mathrm{SO}}|$ at different values of $\alpha$. Furthermore, we wish to investigate the dependence of the critical SO-field required for a switch and corresponding switching times as a function of $\tau_p$ and the pulse shape. For this, a simplified model allows large sweeps in parameter space at low computational cost; thus, we consider a macrospin description where the system consist of two homogeneous antiferromagnetically coupled moments $\mathbf{m}_A$ and $\mathbf{m}_B$. The current-induced SO field is then $\mathbf{H}^{\mathrm{SO}}$ at $\mathbf{m}_A$ and $-\mathbf{H}^{\mathrm{SO}}$ at $\mathbf{m}_B$. Setting $J_{ij} < 0$, $K_{2\perp} < 0$ and using the Gilbert equation [the implicit form of Eq. (2) [25], which is convenient to use for the following derivation], the coupled equations for $\mathbf{m}_A$ and $\mathbf{m}_B$ are:

$$\begin{aligned}\dot{\mathbf{m}}_A = {} & \omega_e[\mathbf{m}_A \times \mathbf{m}_B] + \omega_{2\perp} m_{A,z}[\mathbf{m}_A \times \hat{\mathbf{z}}] \\ & - \omega_{4\perp} m_{A,z}^3[\mathbf{m}_A \times \hat{\mathbf{z}}] - \omega_{4\parallel} m_{A,x}^3[\mathbf{m}_A \times \hat{\mathbf{x}}] \\ & - \omega_{4\parallel} m_{A,y}^3[\mathbf{m}_A \times \hat{\mathbf{y}}] - \gamma[\mathbf{m}_A \times \mathbf{H}^{\mathrm{SO}}] \\ & + \alpha \mathbf{m}_A \times \dot{\mathbf{m}}_A \end{aligned} \tag{3}$$

$$\begin{aligned}\dot{\mathbf{m}}_B = {} & -\omega_e[\mathbf{m}_A \times \mathbf{m}_B] + \omega_{2\perp} m_{B,z}[\mathbf{m}_B \times \hat{\mathbf{z}}] \\ & - \omega_{4\perp} m_{B,z}^3[\mathbf{m}_B \times \hat{\mathbf{z}}] - \omega_{4\parallel} m_{B,x}^3[\mathbf{m}_B \times \hat{\mathbf{x}}] \\ & - \omega_{4\parallel} m_{B,y}^3[\mathbf{m}_B \times \hat{\mathbf{y}}] + \gamma[\mathbf{m}_B \times \mathbf{H}^{\mathrm{SO}}] \\ & + \alpha \mathbf{m}_B \times \dot{\mathbf{m}}_B . \end{aligned} \tag{4}$$

Here, $\omega_e = \frac{2\gamma|J|}{\mu_0\mu_s}$ with $|J| = |4J_1 + J_2|$, $\omega_{2\perp} = \frac{2\gamma|K_{2\perp}|}{\mu_0\mu_s}$, $\omega_{4\perp} = \frac{2\gamma K_{4\perp}}{\mu_0\mu_s}$ and $\omega_{4\parallel} = \frac{2\gamma K_{4\parallel}}{\mu_0\mu_s}$ while the dot denotes the time derivative. It follows that $\mathbf{m}\cdot\mathbf{l} = 0$ and $|\mathbf{l}|^2 + |\mathbf{m}|^2 = 1$. Due to strong exchange interaction, $|\mathbf{m}| \ll |\mathbf{l}|$ (exchange limit). Then, $l^2 \approx 1$ and $\mathbf{l}\cdot\dot{\mathbf{l}} \approx 0$. The system is describable by $\mathbf{m} = (0,0,m_z)$ and $\mathbf{l} = (l_x,l_y,0)$ [verified, e.g., in Figs. 1(c) and 1(d)]. Combining Eqs. (3) and (4) and neglecting the second-order damping terms $\alpha\mathbf{m}\times\dot{\mathbf{m}}$, $\alpha\mathbf{m}\times\dot{\mathbf{l}}$ and $\alpha\mathbf{l}\times\dot{\mathbf{m}}$ in combination with $|\omega_e| \gg |\omega_{2\perp}|$, $|\omega_{4\perp}|$, $|\omega_{4\parallel}|$, $\gamma|\mathbf{l}\cdot\mathbf{H}^{\mathrm{SO}}|$, then $\mathbf{m} \approx -\frac{1}{2\omega_e}\mathbf{l}\times\dot{\mathbf{l}}$ [5] and consequently:

$$\mathbf{l}\times\left\{\ddot{\mathbf{l}} - \omega_R^2\left[l_x^3\hat{\mathbf{x}} + l_y^3\hat{\mathbf{y}}\right] - 2\omega_e\gamma\mathbf{H}^{\mathrm{SO}} + 2\omega_e\alpha\dot{\mathbf{l}}\right\} \approx 0, \tag{5}$$

where $\omega_R = \sqrt{2\omega_e\omega_{4\parallel}}$. In planar cylindrical coordinates $(l_x,l_y) = (\cos\phi,\sin\phi)$ the nontrivial solution of Eq. (5) is found by solving:

$$\begin{aligned}\ddot{\phi} + \frac{\omega_R^2}{4}\sin(4\phi) - 2\omega_e\gamma\left(H_y^{\mathrm{SO}}\cos\phi - H_x^{\mathrm{SO}}\sin\phi\right) \\ + 2\omega_e\alpha\dot{\phi} = 0, \end{aligned} \tag{6}$$

where, if $\mathbf{j} \parallel \hat{\mathbf{x}}$, then $\mathbf{H}^{\mathrm{SO}} = H_y^{\mathrm{SO}}\hat{\mathbf{y}}$ and if $\mathbf{j} \parallel -\hat{\mathbf{y}}$ then $\mathbf{H}^{\mathrm{SO}} = H_x^{\mathrm{SO}}\hat{\mathbf{x}}$. Here, $m_z \approx -\frac{1}{2\omega_e}\dot{\phi}$.

### A. Model validation and comparison to atomistic spin dynamics

In Figs. 2(a)–2(f) we include an example of a comparison between the macrospin description [Eqs. (3) and (4)], Eq. (6), and atomistic spin dynamics. Two cases were considered in the atomistic spin dynamics: a finite sized device [same size as that for Figs. 1(c) and 1(d)] and using periodic boundary conditions (PBCs) along $x,y,z$. Firstly, the macrospin approximation and Eq. (6) are in excellent agreement. Secondly, there is nearly a perfect overlap of $l_{x,y}$ and $m_z$ with the atomistic spin dynamics when PBCs are used [Figs. 2(b), 2(d), and 2(f)]. However, quantitative deviations appear when comparing to atomistic spin dynamics of a finite sized device [Figs. 2(a), 2(c), and 2(e)], meaning that for this device size the rotation is not perfectly coherent. In this case, the deviations are not critical, so we can use Eq. (6). Further, we find that the higher the $\alpha$, the better the correspondence with the atomistic simulations of the finite sized device.

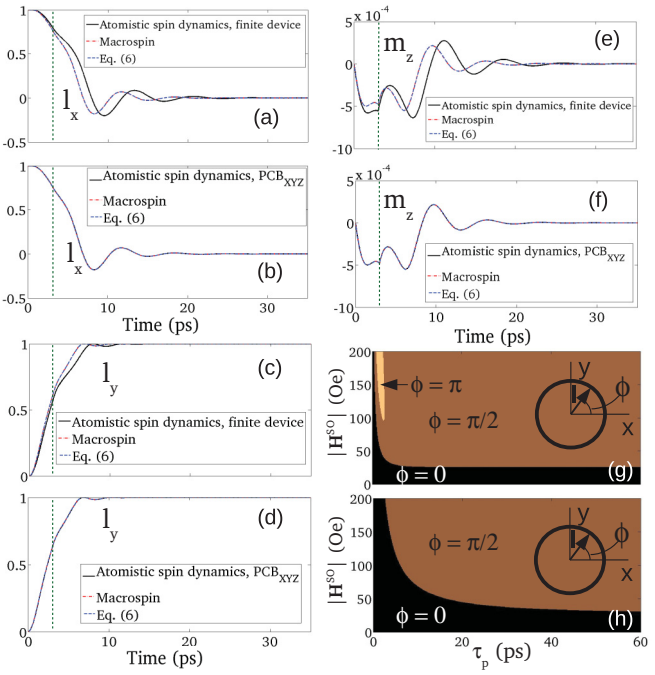


FIG. 2. (a)–(f): Correspondence between atomistic spin dynamics, macro-spin modeling and Eq. (6) when comparing to the finite size device used in Fig. 1 and when imposing PBCs along $x,y,z$ using $150 \times 150 \times 5$ unit cells. (a),(b) $l_x$ vs time, (c),(d) $l_y$ vs time, (e),(f) $m_z$ vs time. The green vertical dashed lines mark the off point of the pulse. In (a)–(f), $\alpha = 0.001$, $\tau_p = 3$ ps, and $|\mathbf{H}^{\mathrm{SO}}| = 40$ Oe. (g),(h): Final angle of $\mathbf{l}$ as a function of $|\mathbf{H}^{\mathrm{SO}}|$ and $\tau_p$ for $\alpha = 0.001$ (g) and $\alpha = 0.01$ (h). Square pulses have been used in all cases.

### B. Overshoot, critical SO-fields, switching times and effects of pulse shape: results and discussion

#### 1. Overshoot characteristics

Using Eq. (6) we investigate the final angle $\phi$ as a function of $|\mathbf{H}^{\mathrm{SO}}|$ and $\tau_p$ for current pulses $\mathbf{j} \parallel \hat{\mathbf{x}}$ (i.e., a single switch event). The starting condition is $\phi = 0$ [$\mathbf{l} = (1,0)$]. Results are shown in Figs. 2(g) and 2(h) for $\alpha = 0.001$ and $\alpha = 0.01$; a very narrow region of overshoot [Fig. 2(g)] occurs for $\alpha = 0.001$ and for these ranges of $|\mathbf{H}^{\mathrm{SO}}|(0 < |\mathbf{j}| \leqslant 10^8\mathrm{A/cm}^2)$ and $\tau_p$. For $\alpha = 0.01$ no overshoot is observed [Fig. 2(h)].

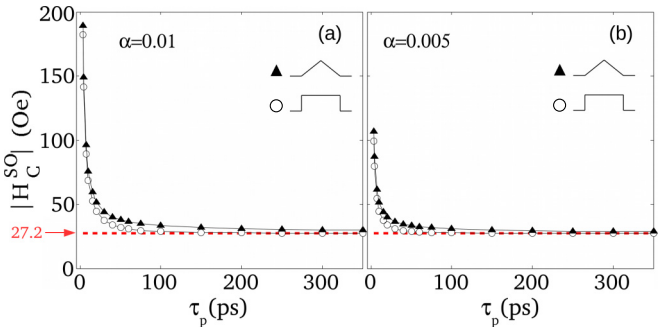


FIG. 3. (a),(b): $|\mathbf{H}_C^{SO}|$ vs $\tau_p$ for different $\alpha = 0.01$(a) and $\alpha = 0.005$(b). The red dotted line and arrow mark the theoretically lowest $|\mathbf{H}_C^{SO}|$. A triangular pulse means that the rise and fall times equals the pulse duration as defined in Fig. 4.

### 2. Critical SO-field for switching and effect of pulse rise and fall time

For a device, a critical parameter is the minimum excitation strength required to write. This, we define as the SO field required to bring $\mathbf{l}$ just over $\phi = \pi/4$, denoted $|\mathbf{H}_C^{SO}|$. Applying Eq. (6), we calculate $|\mathbf{H}_C^{SO}|$ as a function of $\tau_p$ for square and triangular pulses and two $\alpha$ values. Figures 3(a) and 3(b) show results for two dampings. At short pulse durations, a $1/\tau_p$ dependence can be seen, showing smaller $|\mathbf{H}_C^{SO}|$ the lower the $\alpha$. There is however a minimum $|\mathbf{H}_C^{SO}|$ value which is $\alpha$ independent: invoking $m_z \approx -\frac{1}{2\omega_e}\dot{\phi}$ and inserting into Eq. (6) gives $\frac{dm_z}{dt} + 2\omega_e\alpha m_z = \frac{\omega_4}{4}\sin(4\phi) - \gamma H_y^{SO}\cos(\phi)$. For long $\tau_p$ with low current amplitude and/or long pulse rise times, $dm_z/dt \approx 0$ and $2\omega_e\alpha m_z$ is small compared to the anisotropy and SO-field torques. Thus $\frac{\omega_4}{4}\sin(4\phi) - \gamma H_y^{SO}\cos(\phi) \approx 0$. As the requirement for a switch is that $\mathbf{l}$ just overcomes the anisotropy barrier, it suffices to find the smallest $H_y^{SO}$ on the interval $0 \leqslant \phi \leqslant \pi/4$, whereby $\gamma H_y^{SO}\cos(\phi) \geqslant \frac{\omega_4}{4}\sin(4\phi)$ is satisfied. This yields the lower limit for $H_y^{SO} = 27.2$ Oe ($1.36 \times 10^7$A/cm$^2$), which is in excellent agreement to the limits observed in Fig. 3 (horizontal dashed red line).

We now investigate the effect of finite pulse rise and fall times, $\tau_r$, $\tau_f$, respectively, using trapezoidal pulses (defined in Fig. 4) where $\tau_r = \tau_f$. $|\mathbf{H}_C^{SO}|$ is then calculated according to Eq. (6) as a function of $\tau_r/\tau_p$, considering four different $\tau_p$. In Fig. 4(a) results are shown for $\alpha = 0.01$ and in Fig. 4(b), $\alpha = 0.005$. As can be seen, the dependence of $|\mathbf{H}_C^{SO}|$ on $\tau_r/\tau_p$ is not substantial. Thus, pulse shaping is not crucial to achieve a switch at feasible current magnitudes; e.g. even a $\tau_r = \tau_p = 10$ ps (triangular) pulse can switch the device with $|\mathbf{H}_C^{SO}| \sim 45$–$60$ Oe, meaning $\sim$2.25-3 $\times 10^7$A/cm$^2$ if $\alpha = 0.005$–$0.01$. The reason for a higher $|\mathbf{H}_C^{SO}|$ as $\tau_r/\tau_p$ increases is a lower maximum $m_z$ amplitude. The result is a reduced exchange torque.

### 3. Switching times and effect of pulse rise and fall time

In terms of the switching time $\tau_s$, defined here as the time it takes for $l_y$ to reach 90% of its maximum value of 1, the difference can be significant. Figures 4(c) and 4(d) show $\tau_s$ versus $|\mathbf{H}^{SO}|$ for three $\tau_r/\tau_p$ values under a current pulse of

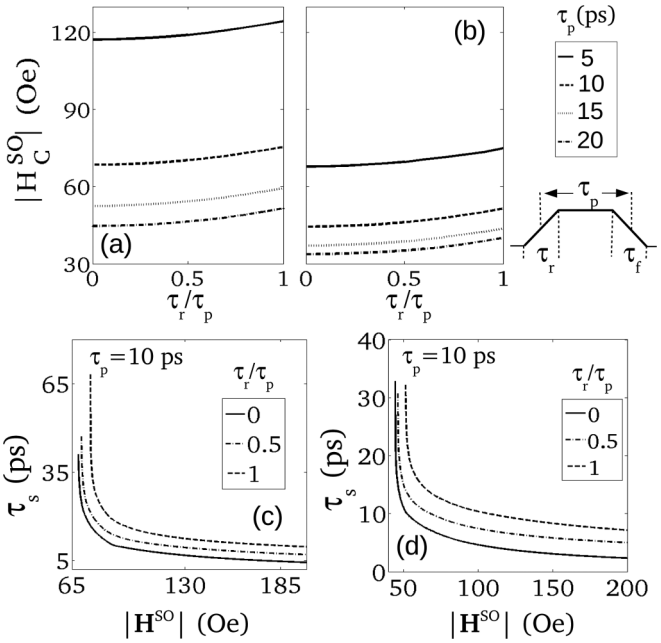


FIG. 4. (a),(b): Dependence of $|\mathbf{H}_C^{SO}|$ on $\tau_r/\tau_p$ for different values of $\tau_p$ and $\alpha$; $\alpha = 0.01, 0.005$ in (a),(b), respectively. The legend for (a),(b) and pulse shape specification is shown to the right ($\tau_r/\tau_p = 0$ means a square pulse and $\tau_r/\tau_p = 1$ is a triangular pulse). (c),(d): $\tau_s$ versus $|\mathbf{H}^{SO}|$ for different $\tau_r/\tau_p$ and a fixed $\tau_p = 10$ ps. In (c), $\alpha = 0.01$ and in (d), $\alpha = 0.005$.

$\tau_p = 10$ ps. Here, two cases are shown in terms of damping; $\alpha = 0.01$ and $\alpha = 0.005$. As long as one is reasonably above $|\mathbf{H}_C^{SO}|$, the behavior is fairly consistent, with a doubling of the switching time as $\tau_r/\tau_p$ approaches 1. The cause is the same as for $|\mathbf{H}_C^{SO}|$ although the effect of lower exchange torque is felt throughout the whole switch event (in determining $|\mathbf{H}_C^{SO}|$ only the time between $0 \leqslant \phi \leqslant \pi/4$ is relevant). For application however, the increase in $\tau_s$ may not be critical as all switching times are still in the picosecond regime.

## C. Switching a uniaxial system

In addition, a uniaxial anisotropy can be induced by strain [16]. Conversely, it should be possible to strain compensate such an anisotropy to recover biaxial dominance. Although more tedious by AMR readout, as an additional tilt of $\mathbf{l}$ during reading is required [8], we include a brief description of switching the uniaxial case between the two 180°-separated stable minima. A schematic of a possible device is shown in Fig. 5(a), patterned such that the uniaxial easy axis (e.a.) is directed at an angle $-\delta$ away from $+\hat{\mathbf{x}}$. Current is injected along $\pm\hat{\mathbf{x}}$, generating a $\mathbf{H}^{SO}||\pm\hat{\mathbf{y}}$ on an $A$ site and $\mathbf{H}^{SO}||\mp\hat{\mathbf{y}}$ on $B$ [Fig. 5(a)]. For a switch, $-\pi/2 < \delta < 0$ and $\mathbf{l}$ only needs to pass $\phi = -\delta + \pi/2$. In the following calculation, a uniaxial term is added to the left side of Eq. (6) as $+\frac{\omega_{R2}^2}{2}\sin(2[\phi + |\delta|])$. Here, $\omega_{R2} = \sqrt{2\omega_e\omega_{2||}}$, $\omega_{2||} = \frac{2\gamma K_{2||}}{\mu_0\mu_s}$, and $K_{2||}$ is the uniaxial anisotropy constant. The derivation of this term follows similar procedures as for the biaxial term and has been derived in, e.g., Ref. [5]. Here, we have computed the time evolution of $\mathbf{l}$ for a single switch in Fig. 5(b). An ultrafast switch

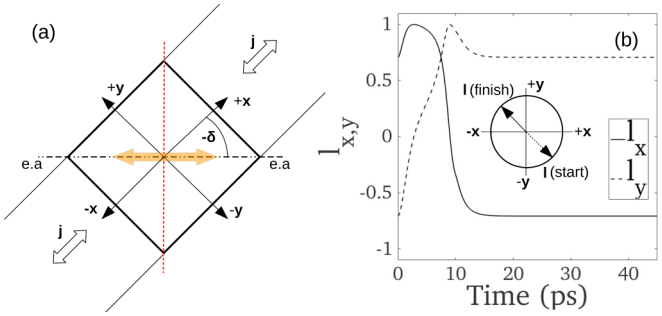


FIG. 5. (a): Schematic of device with uniaxial easy axis (e.a.) at an angle $-\delta$ (here, $-\pi/4$) away from the $+\hat{\mathbf{x}}$ direction. Current and $\mathbf{m}_{A,B}$ directions are indicated by hollow and filled double arrows, respectively. The critical point to overcome for a switch is marked by a red dashed line ($\phi = -\delta + \pi/2$). (b): Time evolution of $\mathbf{l}$ for a square pulse excitation with $\mathbf{H}^{\mathrm{SO}} = 175$ Oe along $+\hat{\mathbf{y}}$, $\alpha = 0.005$, $K_{2\|} = 2.5K_{4\|}$ (ensuring a uniaxial dominance over the biaxial term), and $\tau_p = 10$ ps.

is readily achieved with starting and ending positions of $\mathbf{l}$ at $\phi = -\pi/4$ and $\phi = 3\pi/4$, respectively. One advantage is that, to switch $\mathbf{l}$ to the original position again (not shown here), only the polarity of the current needs to be reversed (whereby $\mathbf{l}$ rotates anticlockwise). Thus, writing only requires one current line. Also in this case, the direction of $\mathbf{H}^{\mathrm{SO}}$ acts in a direction which discourages overshoot of the targeted minima.

## IV. CONCLUSIONS

In conclusion, we have computationally shown robust picosecond writing in easy-plane antiferromagnetic systems with planar biaxial anisotropy and whose symmetry allows for current-induced staggered SO fields. A minimal risk of overshoot due to the fieldlike torque offers an advantage over structures relying on the antidamping torque. Conditions for the lower limit of the switching field have been found. $|\mathbf{H}_C^{\mathrm{SO}}|$ has a rather weak dependence on the rise/fall time of the excitation, while $\tau_s$ can increase up to a factor of two as the pulse shape goes from rectangular to triangular. Ultrafast writing with a dominant uniaxial anisotropy, whereby only one current line is required, has also been demonstrated.

P.E.R. and R.M.O. contributed equally to this work.


[1] I. Fina *et al.*, Nat. Commun. **5**, 4671 (2014).
[2] A. V. Kimel, B. A. Ivanov, R. V. Pisarev, A. Kirilyuk, and Th. Rasing, Nat. Phys. **5**, 727 (2009).
[3] A. V. Kimel, A. Kirilyuk, P. A. Usachev, R. V. Pisarev, and Th. Rasing, Nature (London) **435**, 655 (2005).
[4] S. Wienholdt, D. Hinzke, and U. Nowak, Phys. Rev. Lett. **108**, 247207 (2012).
[5] Ran Cheng, Matthew W. Daniels, Jiang-Gang-Zhu, and Di Xiao, Phys. Rev. B **91**, 064423 (2015).
[6] Helen V. Gomonay and Vadim M. Loktev, Phys. Rev. B **81**, 144427 (2010).
[7] E. V. Gomonay and V. M. Loktev, Low Temp. Phys. **40**, 17 (2014).
[8] T. Jungwirth, X. Marti, P. Wadley, and J. Wunderlich, Nat. Nanotech. **11**, 231 (2016).
[9] Ran Cheng and Qian Niu, Phys. Rev. B **89**, 081105(R) (2014).
[10] A. C. Swaving and R. A. Duine, Phys. Rev. B **83**, 054428 (2011).
[11] Erlend G. Tveten, Alireza Qaiumzadeh, O. A. Treiakov, and Arne Braatas, Phys. Rev. Lett. **110**, 127208 (2013).
[12] Kjetil M. D. Hals, Yaroslav Tserkovnyak, and Arne Braatas, Phys. Rev. Lett. **106**, 107206 (2011).
[13] J. Železný, H. Gao, K. Výborný, J. Zemen, J. Mašek, Aurelien Manchon, J. Wunderlich, Jairo Sinova, and T. Jungwirth, Phys. Rev. Lett. **113**, 157201 (2014).
[14] S. D. Ganichev, Int. J. Mod. Phys. B **22**, 1 (2008).
[15] Sergii Khmelevskyi and Peter Mohn, Appl. Phys. Lett. **93**, 162503 (2008).
[16] A. B. Schick, S. Khmelevskyi, O. N. Mryasov, J. Wunderlich, and T. Jungwirth, Phys. Rev. B **81**, 212409 (2010).
[17] V. M. T. S. Barthem, C. V. Colin, H. Mayaffre, M.-H. Julien, and D. Givord, Nat. Commun. **4**, 2892 (2013).
[18] Han-Chun, Zhi-Min Liao, R. G. Sumesh Sofin, Gen Feng, Xin-Mei Ma, Alexander B. Shick, Oleg N. Mryasov, and Igor V. Shvets, Adv. Mater. **24**, 6374 (2012).
[19] F. Maca, J. Masek, O. Stelmakhovych, X. Marti, H. Reichlova, K. Uhlirova, P. Beran, P. Wadley, V. Novak, and T. Jungwirth, J. Magn. Magn. Mater. **324**, 1606 (2012).
[20] P. Wadley *et al.*, Nat. Commun. **4**, 2322 (2013).
[21] P. Wadley *et al.*, Science **351**, 587 (2016).
[22] M. Jourdan, H. Brauning, A. Sapozhnik, H.-J. Elmers, H. Zabel, and M. Klaui, J. Phys. D: Appl. Phys. **48**, 385001 (2015).
[23] P. Wells and J. H. Smith, Acta Crystallogr. Sect. A **26**, 379 (1970).
[24] Vitoria M. T. S. Barthem, Claire V. Colin, Richard Haettel, Didier Defeu, and Dominique Givord, J. Magn. Magn. Mater. **406**, 289 (2016).
[25] Thomas Schrefl, Josef Fidler, Rok Dittrich, Dieter Suess, Werner Scholtz, Vassilios Tsiantos, and Hermann Forster, in *Spin Dynamics in Confined Magnetic Structures II, Topics in Applied Physics* Vol. 87, edited by B. Hillebrands and K. Ounadjela (Springer-Verlag, Berlin, Heidelberg, 2003), Chap. 1.
[26] R. F. L. Evans, W. J. Fan, P. Chureemart, T. A. Ostler, M. O. A. Ellis, and R. W. Chantrell, J. Phys.: Condens. Matter **26**, 103202 (2014).
[27] R. Masrour, E. K. Hlil, M. Hamedoun, A. Benyoussef, A. Bouahar, and H. Lassri, J. Magn. Magn. Mater. **393**, 600 (2015).
[28] W. H. Press, B. P. Flannery, S. A. Teukolsky, and W. T. Vettering, *Numerical Recipes: The Art of Scientific Computing* (Cambridge University Press, Cambridge, England, 1988).